Synthesis of Co-containing mesoporous carbon foams using a new cobalt-oxo cluster as a precursor

Yao-Kang Lv [a], Yun-Long Feng [b], Li-Hua Gan [a,*], Ming-Xian Liu [a], Liang Xu [a], Cao Liu [a],
Hao-Wen Zheng [a], Jie Li [a]

[a] Department of Chemistry, Tongji University, 1239 Siping Road, Shanghai 200092, PR China
[b] Zhejiang Key Laboratory for Reactive Chemistry on Solid Surfaces, Institute of Physical Chemistry, Zhejiang Normal University, Jinhua, Zhejiang 321004, PR China

ABSTRACT

A novel trinuclear cobalt-oxo cluster $2[Co_3O(Ac)_6(H_2O)_3] \cdot H_2O$ (**Co-OXO**) has been obtained and characterized by X-ray single-crystal diffraction and elemental analysis. The structure of **Co-OXO** displays 3D supramolecular networks through hydrogen bonds and generates boron nitride (**bnn**) topology. **Co-OXO** was further used as a precursor to synthesize Co-containing mesoporous carbon foams (Co-MCFs), which exhibit highly ordered mesostructure with specific surface area of 614 $m^2\,g^{-1}$ and uniform pore size of 2.7 nm. Charge–discharge tests show that the specific discharge capacitance of Co-MCFs is 7% higher than that of the MCFs at the current density of 100 $mA\,g^{-1}$, and 26% higher than that of MCFs at the current density of 3 $A\,g^{-1}$. The electrochemical behaviors of Co-MCFs are obviously improved due to the improved wettability, increased graphitization degree and the pseudo-capacitance through additional faradic reactions arising from cobalt.

© 2011 Elsevier Inc. All rights reserved.

1. Introduction

Porous carbon materials possess excellent chemical, physical and thermal stability, thus they are appealing for sensor, membrane, separation, catalyst, energy conversion and storage [1–11]. Traditional porous carbon materials such as activated carbons are one of the favored choices of supercapacitor electrode materials. However, it is well known that traditional methods of producing porous carbons from either natural precursors such as coconut shell or synthetic precursors such as phenolic resin do not offer sufficient control over porosity. Therefore, even if these carbons have a sufficiently large surface area, their application in supercapacitors is limited by their intrinsically small micropores. The micropores are less easily wetted by electrolytes, and ionic motion in such small pores is not facilitated, such that the high-rate capability, which is one of the inherent advantages of supercapacitors, may not be realized [11]. At present, mesoporous carbon foams (MCFs) attract broad attention due to their high specific surface areas, well-defined structures and appropriate pore size for quick mass transfer and ion diffusion [12–16]. However, the specific capacitances of MCFs are still low especially at high current density due to their limited electrical conductivity

and relatively inert surface [17,18]. It is known that besides the influences of the pore structure on the capacitor behaviors, the texture of materials can also change the capacitor behaviors. In order to enhance the electrochemical properties, various compounds were introduced into the MCFs, which not only improve the wettability of the interface between electrolyte and electrodes, but also introduce pseudocapacitive effects [19–24]. For instance, loading or doping metals or metal oxides in the MCFs have been reported and proved to have a higher capacitance, but the poor dispersion of metal oxides in the MCFs usually leads to the detriment of their electrochemical properties [22–24].

Metal-oxo clusters represent a class of compounds that offer a large variety of candidates to elaborate hybrid materials by the nanobuilding blocks approach [25–28]. In addition to their remarkable chemical and physical properties, they have various application fields such as catalysis, medicine and material science [29–32]. Herein we report a novel trinuclear cobalt-oxo cluster $2[Co_3O(Ac)_6(H_2O)_3] \cdot H_2O$ (HAc=acetic acid) (**Co-OXO**), in view of the advantages of cobalt-oxo clusters as functional nanobuilding blocks, we employed **Co-OXO** as a precursor to prepare Co-containing mesoporous carbon foams (Co-MCFs) through an amphiphilic surfactant-templating approach.

To the best of our knowledge, using a cobalt-oxo cluster as a precursor to prepare Co-MCFs is reported for the first time. During the carbonization process, **Co-OXO** was transformed into metallic cobalt embedded in the carbon matrix, and the electrode

---

synthesized by Co-MCFs can be used in 7 mol L^{-1} KOH electrolyte. The mesostructures of Co-MCFs were investigated by XRD patterns, N$_2$ sorption and TEM. Cyclic voltammetry and charge–discharge tests indicate that, in comparison with pure MCFs, Co-MCFs exhibit higher capacitance and fast charge–discharge characteristics result from the improvement of graphitization, surface wettability and pseudo-capacitive effect of cobalt.

2. Experimental sections

2.1. Materials and measurements

All starting reagents were purchased commercially and used without further purification. Elemental analyses were performed on a Perkin−Elmer 2400II elemental analyzer. Powder X-ray diffraction (XRD) experiments were taken on a Bruker D8 Advance diffractometer with Cu $K\alpha$ ($\lambda = 0.154056$ Å) radiation. Raman spectra were obtained using a Renishaw Invia. system, under $\lambda_{exc} = 514$ nm laser excitation. Thermal gravimetric analysis (TGA) was carried out using a Netzsch STA 449C thermoanalysis instrument in the temperature range of 303–1173 K. The sample was heated up to 1173 K with a heating rate of 5 K min^{-1} under air atmosphere. Nitrogen adsorption/desorption isotherms were measured at the liquid nitrogen temperature using a Micromeritics Tristar 3000 analyzer. Transmission electron microscopic (TEM) observations were conducted on a JEOL2100 microscope operated at 200 kV.

2.2. Synthesis of 2[Co$_3$O(Ac)$_6$(H$_2$O)$_3$]·H$_2$O (**Co-OXO**)

0.498 g Co(Ac)$_2$·4H$_2$O (2.00 mmol), 0.240 g HAc (4.00 mmol), 40 ml of EtOH and 15 ml of 30% H$_2$O$_2$ were mixed and stirred at 60 °C for 4 h, the resulted pink solution was kept at 20 °C. Dark pink block crystals of **Co-OXO** suitable for X-ray crystallographic study were obtained via slow evaporation in 2 weeks. Yield: 86% on the basis of Co(Ac)$_2$·4 H$_2$O. Elemental analysis (%) calculated for C$_{24}$H$_{50}$Co$_6$O$_{33}$: C, 23.62%; H, 4.13%; found: C, 23.68%; H, 4.24%.

2.3. Preparation of Co-MCFs and MCFs

Co-MCFs were prepared using resol as an organic precursor, NaOH as a catalyst, complex **Co-OXO** as a functional precursor and triblock copolymers Pluronic F127 ($M_w = 12,600$, EO$_{106}$−PO$_{70}$−EO$_{106}$) as a template. The resol was prepared according to the procedure described in the literature [2]. Typically, 0.03 g **Co-OXO** and 1.0 g of F127 was dissolved in 20 g of 4:1 mass ratio of ethanol and water mixture. Then the ethanol solution of resol containing 0.61 g of phenol and 0.39 g of formaldehyde was added into the above mixture. A homogeneous pink solution was obtained after stirring for 30 min. The solution was coated as a thin polymer membrane on the surface of dish and the membrane was kept at 25 °C for 8 h. Thermal polymerization of the membrane was carried out at 100 °C for 12 h. The thin membrane was crushed into powder and carbonized at 900 °C in a purified nitrogen flow with a heat rate of 1 °C min^{-1} to produce Co-MCFs. As a comparison, we synthesized MCFs by similar approach without adding cobalt precursor.

2.4. Single-crystal structure determination

The data collection of complex **Co-OXO** was performed on a Bruker APEX II diffractometer equipped with a graphite-monochromatized Mo−Kα radiation ($\lambda = 0.71073$ Å) at 296 K. Data intensity was corrected by Lorentz-polarization factors and

Table 1
Crystal data and structure refinement for 1.

Complexes	1
Empirical formula	C$_{24}$H$_{50}$Co$_6$O$_{33}$
Formula weight	1220.22
Crystal system	Monoclinic
Space group	$C2/c$
a (Å)	27.0265(6)
b (Å)	13.8344(2)
c (Å)	15.2810(4)
β (deg)	123.277(2)
V (Å^3)	4776.6(6)
Z	4
D/g (cm^{-3})	1.697
μ (mm^{-1})	2.130
GOF on F^2	0.991
$R1$, $wR2$ [$I > 2\alpha(I)$]	0.0734, 0.1803
$R1$, $wR2$ (all data)	0.1219, 0.2025

$R1 = [\Sigma|F_o| - |F_c|]/[\Sigma|F_c|]$. $wR2 = \{[\Sigma w(F_o^2 - F_c^2)^2]/[\Sigma w(F_o^2)^2]\}^{1/2}$.

Table 2
Selected bond lengths (Å) and bond angles (deg.) for 1.

Co1–O1	2.004(2)	Co2–O6	2.015(2)
Co1–O3	2.016(2)	Co2–O7	2.024(2)
Co1–O4	2.031(2)	Co2–O1W	2.107(3)
Co1–O5	2.046(2)	Co3–O1	1.962(2)
Co1–O2	2.0476(19)	Co3–O13	2.020(2)
Co1–O2W	2.099(3)	Co3–O11	2.026(2)
Co2–O1	1.940(2)	Co3–O10	2.032(2)
Co2–O9	2.006(2)	Co3–O12	2.039(2)
Co2–O8	2.013(2)	Co3–O3W	2.130(3)
O1–Co1–O3	93.08(10)	O8–Co2–O7	87.28(9)
O1–Co1–O4	92.51(9)	O6–Co2–O7	174.39(11)
O3–Co1–O4	174.40(11)	O1–Co2–O1W	178.75(9)
O1–Co1–O5	91.89(9)	O9–Co2–O1W	86.17(10)
O3–Co1–O5	87.0(1)	O8–Co2–O1W	85.41(9)
O4–Co1–O5	93.24(10)	O6–Co2–O1W	87.26(9)
O1–Co1–O2	92.61(8)	O7–Co2–O1W	87.13(9)
O3–Co1–O2	91.87(9)	O1–Co3–O13	93.63(9)
O4–Co1–O2	87.45(9)	O1–Co3–O11	92.27(9)
O5–Co1–O2	175.41(10)	O13–Co3–O11	173.47(10)
O1–Co1–O2W	178.81(8)	O1–Co3–O10	94.26(9)
O3–Co1–O2W	86.97(10)	O13–Co3–O10	88.73(10)
O4–Co1–O2W	87.45(10)	O11–Co3–O10	88.05(11)
O5–Co1–O2W	86.93(9)	O1–Co3–O12	94.20(9)
O2–Co1–O2W	88.57(9)	O13–Co3–O12	89.04(10)
O1–Co2–O9	94.93(10)	O11–Co3–O12	93.31(11)
O1–Co2–O8	93.49(9)	O10–Co3–O12	171.37(10)
O9–Co2–O8	171.57(11)	O1–Co3–O3W	177.44(9)
O1–Co2–O6	92.20(9)	O13–Co3–O3W	88.89(9)
O9–Co2–O6	86.70(9)	O11–Co3–O3W	85.22(9)
O8–Co2–O6	92.42(9)	O10–Co3–O3W	86.19(10)
O1–Co2–O7	93.41(9)	O12–Co3–O3W	85.44(10)
O9–Co2–O7	92.77(9)		

empirical absorption. The structure was solved by direct methods and expanded with difference Fourier techniques. All non-hydrogen atoms were refined anisotropically. The hydrogen atoms on oxygen atoms were located from the difference Fourier maps and the hydrogen atoms on carbon atoms were generated geometrically. All calculations were performed using SHELXS-97 and SHELXL-97 [33,34]. Further details for structural analyses are summarized in Table 1, selected bond lengths and angles are listed in Table 2, and the hydrogen bond distances and bond angles are listed in Table 3. CCDC-745977 contains the crystallographic data in CIF format.

2.5. Electrochemical evaluation

The electrochemical measurements were done in a three-electrode experimental setup. The electrolyte was a 7 mol L^{-1} KOH aqueous solution. Saturated calomel electrode (SCE) was used as reference electrode, and nickel foams as the counter-electrode. The working electrode was prepared as following: Co-MCFs or MCFs were mixed with polytetrafluoroethylene and

graphite powder with a mass ratio of 8.5:1:0.5. The mixture was pressed between two pieces of nickel foams under 30 MPa. Thereafter, the 0.50 mm thick electrode was dried overnight at 100 °C. All electrochemical measurements were performed on CHI 660D electrochemical workstation, and the potential window was chosen in the range of −0.8 to 0 V versus SCE.

3. Results and discussion

3.1. Crystal structure of **Co-OXO**

Single crystal X-ray diffraction analysis shows that complex **Co-OXO** is monoclinic space group C2/c. Each asymmetric unit contains three crystallographic independent cobalt atoms, one μ_3-O, six Ac$^-$ ligands, three coordinated water molecules and a half of lattice water molecule. As shown in Fig. 1, Co1 is coordinated by four carboxyl oxygen atoms from four different Ac$^-$ ligands (Co1–O 2.016(2)–2.048(6) Å), one oxygen atom from the μ_3-O (Co1–O 2.004(2) Å), and one water molecule (Co1–O 2.099(3) Å) in distorted octahedral geometry. Co2 and Co3 also adopt the slightly distorted octahedral coordination geometry with four carboxyl oxygen atoms, one μ_3-O and one water molecule. The average bond length of Co2–O and Co3–O are close to that of Co1–O, and they are comparable to those in the previously reported compound [35–38]. It is noteworthy that the trinuclear cobalt-oxo cluster has a pseudo-C3 axis on the central μ_3-O perpendicular to the Co–Co plane and the Co···Co distances bridged by the μ_3-O are 3.408(2), 3.397(4), and 3.426(5) Å, respectively. Furthermore, there are multiple intermolecular O–H···O hydrogen bonds that connect the neighboring clusters to construct a 3D framework (Fig. 2). Better insight of this 3D hydrogen bond network can be achieved by topology analysis. As shown in Fig. 3, each cobalt-oxo cluster is linked to five neighboring clusters through hydrogen bonds to represent a 5-connected node (Fig. 3a), and the non-interpenetrating uninodal 5-connected net is shown in Fig. 3b. It has the well-known boron nitride (**bnn**) topology with the Schläfli symbol of (4^6. 6^4) and the vertex symbol for this net is 4.4.4.4.4.4.6.6.6.*. [39–41].

3.2. Structure of mesoporous carbon foams

Generally, the electrical energy of MCFs as supercapacitors mainly stored in the form of electrical double-layer capacitance is attributed to the accumulation of charges at the electrode/

Table 3
Hydrogen bond distances (Å) and bond angles (deg.) for 1.

D–H···A	d(D–H)	d(H···A)	d(D···A)	<(DHA)
O1W–H1WA···O5#1	0.810(8)	2.395(17)	2.965(3)	128.2(17)
O1W–H1WB···O6#2	0.813(10)	2.334(9)	3.101(3)	157.7(14)
O1W–H1WB···O9#2	0.813(10)	2.588(12)	3.206(3)	134.(1)
O2W–H2WA···O7#3	0.823(8)	2.457(13)	3.116(3)	137.8(17)
O2W–H2WA···O8#3	0.823(8)	2.468(13)	3.213(3)	151.0(15)
O2W–H2WB···O11#4	0.815(10)	2.295(10)	3.021(3)	148.7(16)
O3W–H3WA···O5W#5	0.876(11)	2.428(14)	3.213(10)	149.4(9)
O3W–H3WB···O2#6	0.887(9)	2.076(10)	2.925(3)	159.8(13)
O5W–H5WB···O4W#7	0.815(13)	2.198(19)	2.886(13)	142.(3)

Symmetry codes: (#1) x, 1−y, 0.5+z; (#2) −x, y, 0.5−z; (#3) x, 1−y, −0.5+z; (#4) 0.5−x, 0.5+y, 0.5−z; (#5) x, −y, −0.5+z; (#6) 0.5−x, −0.5+y, 0.5−z; (#7) 0.5−x, 0.5−y, 1−z.
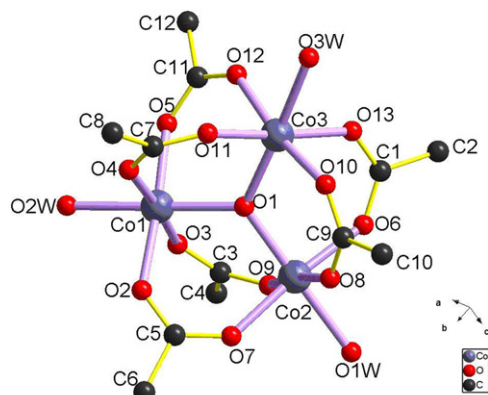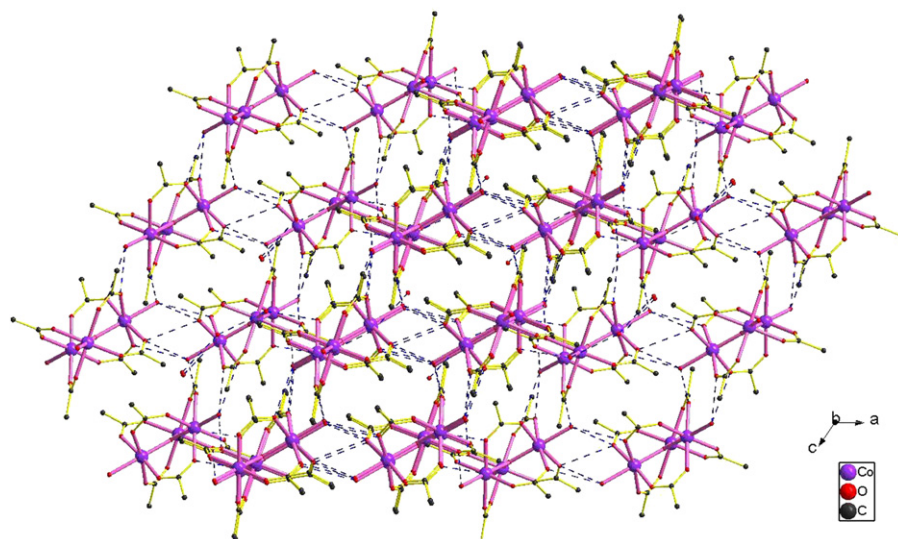

Fig. 1. Structure of **1** showing the atom labeling, all the hydrogen atoms and lattice water molecules are omitted for clarity.

Fig. 2. View down the b axis of the 3-D supramolecular network of **1**, showing the hydrogen bonding interactions (broken lines), all H atoms and are omitted for clarity.
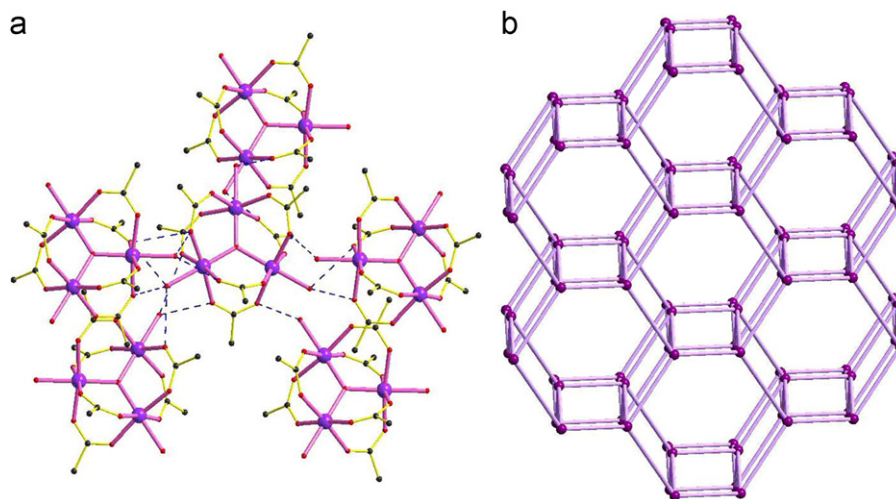
Fig. 3. A5-connected cobalt-oxo cluster linked with five neighboring clusters (a); schematic representation of the 5-connected **bnn** network of **1** (b).
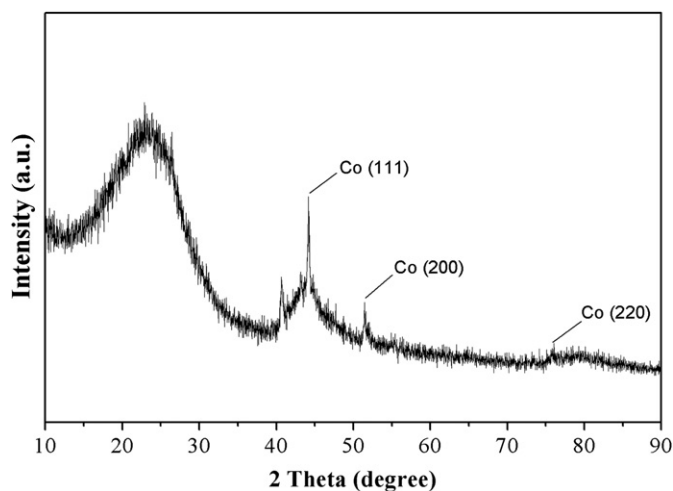

Fig. 4. Wide-angle XRD patterns of Co-MCFs.

Fig. 5. Small-angle XRD patterns of Co-MCFs.

electrolyte interface. Recently, Gogotsi et al. and Simon et al. investigated the relationship between the pore sizes of the carbon electrodes and ion sizes of the electrolyte for supercapacitors, their works indicated that the pore size leading to the maximum double-layer capacitance is very close to the ion size, and for fast charge–discharge processes such as pulse power applications, increasing the pore size might be beneficial [42–44]. The morphology and the pore structure of MCFs may critically affect their electrochemical properties, specially serving as an electrode material involving the electrolyte accessibility, ion transportation, electron conductivity, etc.

Fig. 4 gives the wide-angle XRD patterns of Co-MCFs, showing that **Co-OXO** was reduced to metallic cobalt during the carbonization process at 900 °C. The diffraction peaks at $2\theta = 44.2°$ (111), 51.5° (200), and 75.9° (220) can be indexed to the characteristic peaks of cobalt phase (PDF#15-0806) with the cubic $Fm3m$ structure. However, the peak at 41° is not unlabeled and unassigned because it is not related with known cobalt, cobalt oxides, cobalt carbide or common cobalt salt, this problem need further investigation. Beside the characteristic peaks, two broad diffraction peaks located around 24° and 44° are observed which correspond to the diffractions for carbon. These results indicate that **Co-OXO** was transformed into metallic cobalt and incorporated in the carbon matrix during the carbonization process [9,10]. The average size of the cobalt nanoparticles was founded to be 25 nm according to the broadening of
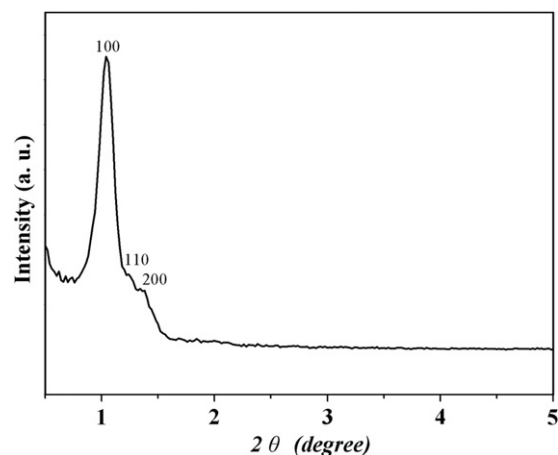
the full width at half-maximum of the (1 1 1) diffraction peak by Scherrer's equation.

Fig. 5 exhibits the small-angle XRD patterns of Co-MCFs. It can be seen that the sample exhibits a strong peak at $2\theta = 1.04°$ which indicates that Co-MCFs have uniform mesopores.

Fig. 6 shows the nitrogen adsorption–desorption isotherms and pore size distribution curves. The isotherms of Co-MCFs shows representative type IV [45] curves which exhibit a sharp capillary condensation step at relative pressures of 0.4–0.6, corresponding to the narrow pore size distribution. The Co-MCFs possess the Brunauer–Emmett–Teller (BET) specific surface area of around 614 m^2 g^{-1}. The pore size distribution of Co-MCFs is calculated from the desorption branch of the isotherm using the Barrett–Joyner–Halenda (BJH) method, and it exhibits single pores with the most probable pore size of 2.7 nm. For comparison, MCFs possess a BET specific surface area of 664 m^2 g^{-1} and pore size of 2.8 nm. TGA conducted in air indicated that the amount of cobalt in the Co-MCFs was around 2 wt% (Fig. 7). These results reveal that approximate 2% mass ratio of cobalt was embedded in the carbon matrix, the incorporation of cobalt has no obvious influence on the pore structure of Co-MCFs, and Co-MCFs have mesoporous structure with uniform pore size.

Previous literatures reported cobalt-doped mesoporous carbon materials, which were synthesized using silica template [9,10]. This method is complex, and several toxic compounds such as HF were used to remove the silica frameworks. Since the cobalt

clusters of **Co-OXO** are neutral and chelated by acetate groups, the aggregation and condensation of cobalt species were restricted during the co-assembly procedure of **Co-OXO** and resol, thus resulting in the cooperative assembly and subsequent curing of ordered mesostructures with high cobalt dispersion. Fig. 8
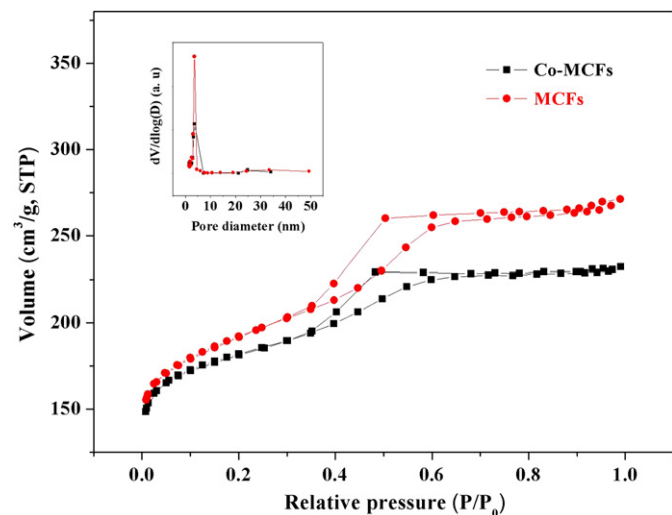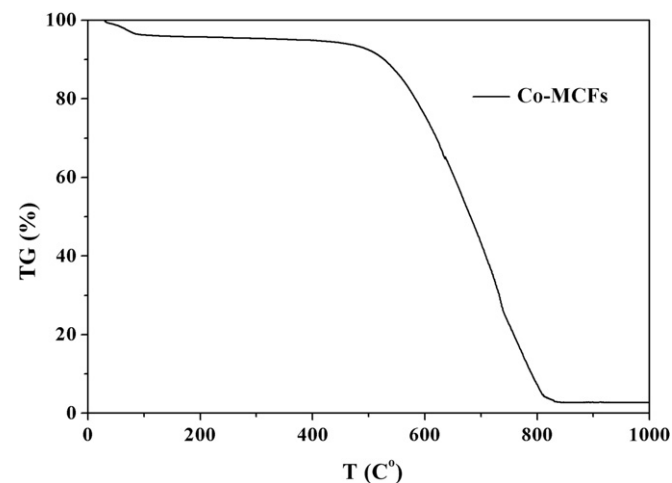
shows the TEM images of Co-MCFs, which indicate that Co-MCFs have uniform mesopores and the individual pore size is around 3 nm, this result matches the results of nitrogen sorption analyses and the small-angle XRD patterns. The dark spots observed in TEM images are the cobalt nanoparticles. The size of large particles of cobalt we find through TEM images is between 10 nm and 30 nm. Thus the method reported here is an effective strategy for the incorporation of cobalt nanoparticles into mesoporous carbon foams.

3.3. Graphitization degree of mesoporous carbon foams

The Raman spectra of Co-MCFs and MCFs are displayed in Fig. 9. The spectra show a distinct pair of broad bands near $1580\ cm^{-1}$ (G band) and $1337\ cm^{-1}$ (D band). The G band and D band assign to the hexagonal carbon plane and crystal defects or imperfections, respectively. The ratio of the relative intensity of these two bands (I_D/I_G) is proportional to the number of defect sites in the graphite carbon. The lower the ratio is, the higher the graphitization is. It can be calculated that the I_D/I_G ratio declines from 1.07 (MCFs) to 0.92 (Co-MCFs), which shows that the graphitization degree of Co-MCFs increased in comparison with MCFs. It is well known that Group VIII metal such as cobalt compounds are graphitization catalysts [46–49]; introducing complex **Co-OXO** as a precursor to obtain Co-MCFs with good cobalt dispersion could accelerate the development of graphitic structure of mesoporous carbon foams more evenly and effectively.
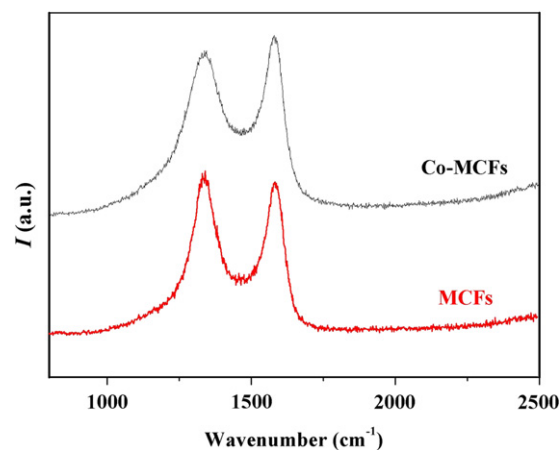

Fig. 6. Nitrogen adsorption and desorption isotherms and the pore size pore size distributions (insert) of Co-MCFs and MCFs.

Fig. 7. TG curve for Co-MCFs.

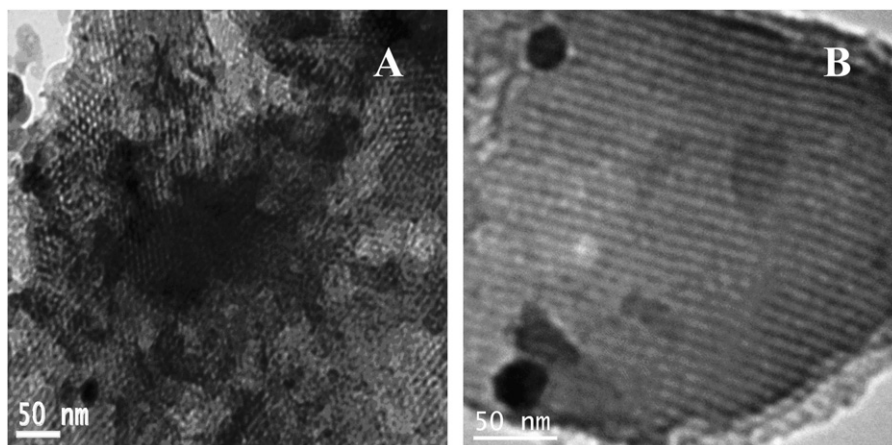
Fig. 9. Raman spectra of Co-MCFs and MCFs.

Fig. 8. TEM image of Co-MCFs.

3.4. Surface wettability properties of mesoporous carbon foams

The surface wettability of Co-MCFs and MCFs were investigated by the measurement of the water contact angle. Fig. 10 shows the shapes of a water droplet on the surface of Co-MCFs and MCFs. The contact angle of Co-MCFs for water is about $110.2 \pm 1.5°$, obviously lower than that of MCFs ($130.7 \pm 1.5°$), which shows that the surface wettability of Co-MCFs is improved in comparison with MCFs.

3.5. Electrochemical properties of mesoporous carbon foams

The electrochemical performances of Co-MCFs and MCFs were investigated by cyclic voltammetry (CV), electrochemical impedance spectroscopy (EIS) and galvanostatic charge–discharge techniques. Fig. 11 shows the CV curves of Co-MCFs and MCFs electrodes. The CV curves of Co-MCFs were characterized with rectangle-like shape at sweep rates from 5 to 50 mV s^{-1}, which indicate ideal capacitance behaviors in charging–discharging processes. However, the CV curve of MCFs veers away much from rectangle-shape at scanning rate of 50 mV s^{-1}, suggesting resistance-like electrochemical behavior. The improvement of CV performances of Co-MCFs should be ascribed to their higher graphitization degree and consequent improved electrical conductivity [46], which is confirmed by the Raman spectra. The capacitance of material is in proportion to the areas of its CV curves. The specific capacitance values calculated from Fig. 11 are presented in Table 4. The specific capacitances of

Table 4
Capacitance values of MCFs and Co-MCFs measured by cyclic voltammetry in 7 mol L^{-1} KOH solution.

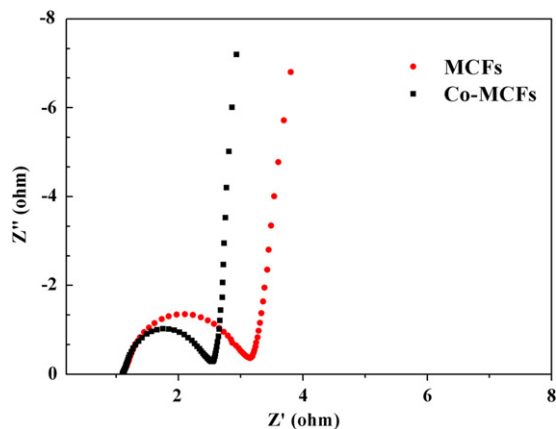| Scanning rate/ (mV s^{-1})	Capacitance/(F g^{-1})	
	MCFs	Co-MCFs
5	97.9	102.0
10	88.7	97.9
20	78.3	92.6
50	53.7	83.0

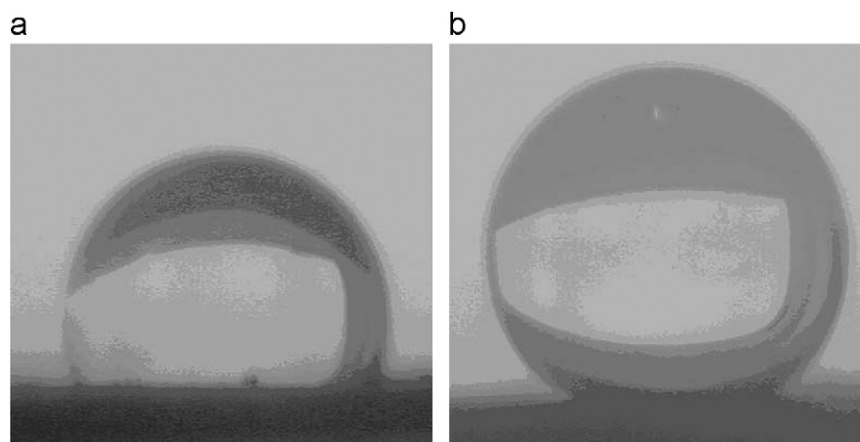**Fig. 12.** Impedance spectroscopy of MCFs and Co-MCFs.

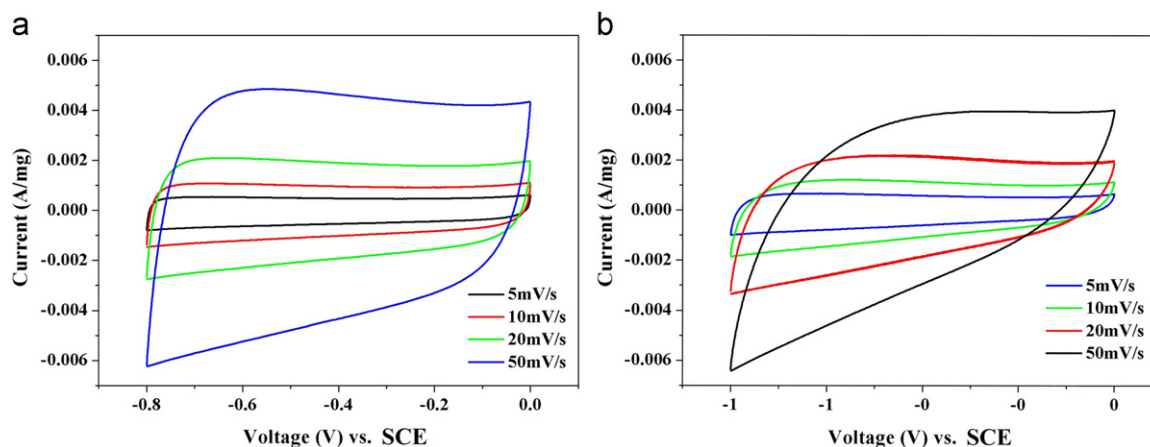**Fig. 10.** Photographs of water droplet on the surface of Co-MCFs (a) and MCFs (b).

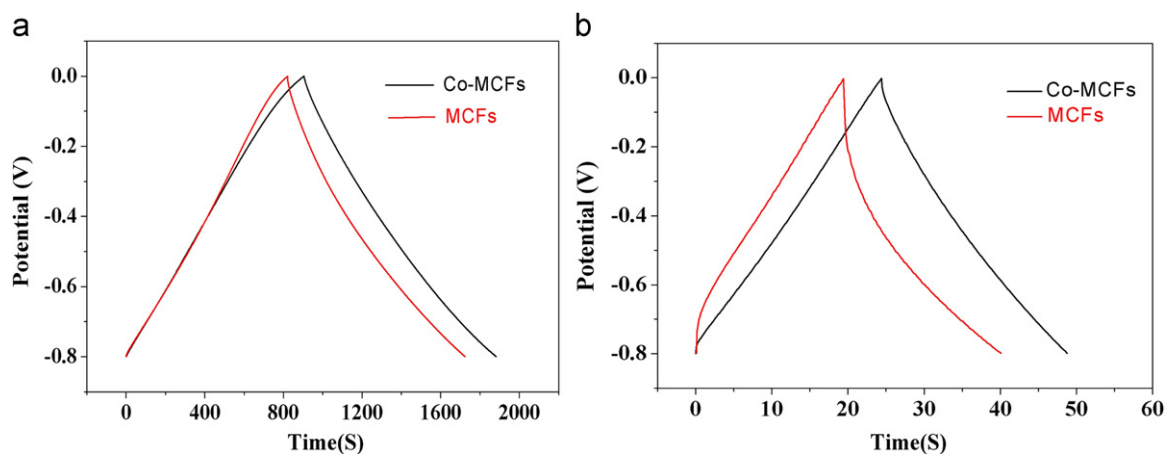**Fig. 11.** Cyclic voltammetry curves of (a) Co-MCFs and (b) MCFs.

Fig. 13. Galvanostatic charge-discharge curves of the Co-MCFs and MCFs electrodes at the loading current density of (a) 100 mA g^{-1} (b) 3 A g^{-1}.

MCFs and Co-MCFs were 97.9 F g^{-1} and 102 F g^{-1} at scanning rate of 5 mV s^{-1}, and their specific capacitances were 54 F g^{-1} (MCFs) and 83 F g^{-1} (Co-MCFs) at scanning rate of 50 mV s^{-1}. The specific capacitance of Co-MCFs is larger than that of MCFs especially at higher scanning rate. The enhancement of the electrochemical properties is attributed to improved wettability and consequent enhancement of surface contact of electrolyte and carbon, increased graphitization degree, as well as the pseudo-capacitance through additional faradic reactions arising from cobalt.

The impedance spectra of Co-MCFs and MCFs electrode materials at the potential of 0 V are shown in Fig. 12. In the low frequency region, the impedance plot increases with a nearly vertical line, indicating a good capacitive performance. It can be seen that the internal resistance of Co-MCFs is smaller than that of MCFs, which suggests that the Co-MCFs electrode has better conductive properties and consequent electrochemical properties. This result matches those of the CV curves.

The galvanostatic charge–discharge behavior reflects substantially electrical energy storage. Based on the results of charge–discharge cycling, the specific discharge capacitance of a single electrode in the capacitors can be calculated according to the equation: $C=(I \times \Delta t_d)/(m \times \Delta V)$ where i is the constant current (A), m is the mass of the activated substance (g), Δt_d is the discharging time (s), and ΔV is the potential change (V). The potential range we used to estimate was -0.2 V to -0.6 V. As shown in Fig. 13, both Co-MCFs and MCFs electrodes present linear galvanostatic charge–discharge curves at the loading current density of 100 mA g^{-1}. The calculated specific capacitance of the Co-MCFs reaches 120.5 F g^{-1}, 7% higher than that of the MCFs (112.8 F g^{-1}) (Fig. 13a). With the increase of current densities to 3 A g^{-1}, the specific capacitance of Co-MCFs decreases to 95.2 F g^{-1}, 26% higher than that of MCFs which is 75.7 F g^{-1} (Fig. 13b). It can also be seen that Co-MCFs electrode possesses an obviously smaller 'IR drop' at the beginning of discharge compared with MCFs, and the symmetricity of charge–discharge curve of Co-MCFs at the current density of 3 A g^{-1} is much better than that of MCFs. These results proved that the specific capacitance of Co-MCFs was significantly improved in comparison with MCFs, especially at high current density.

4. Conclusion

In summary, we first report a trinuclear cobalt-oxo cluster 2[Co$_3$O(Ac)$_6$(H$_2$O)$_3$]·H$_2$O (**Co-OXO**). The structure of **Co-OXO** displays 3D supramolecular networks through hydrogen bonds and generates boron nitride (bnn) topology. **Co-OXO** was further

used as a precursor to synthesize Co-MCFs, which exhibit highly ordered mesostructure with specific surface area of 614 m^2 g^{-1} and uniform pore size of 2.7 nm. Compared with MCFs, Co-MCFs exhibit higher specific discharge capacitance and much better fast charge-discharge behavior, which are attributed to the improved wettability, increased graphitization degree and the pseudo-capacitance through additional faradic reactions arising from cobalt. It can be expected that Co-MCFs have a promising application in supercapacitors.

Appendix A. Supporting information

Supplementary data associated with this article can be found in the online version at doi:10.1016/j.jssc.2011.11.010.

References

[1] M.X. Liu, L.H. Gan, C. Tian, J.C. Zhu, Z.J. Xu, Z.X. Hao, L.W. Chen, Carbon 45 (2007) 3045–3046.
[2] Y. Meng, D. Gu, F.Q. Zhang, Y.F. Shi, H.F. Yang, Z. Li, C.Z. Yu, B. Tu, D.Y. Zhao, Angew. Chem. Int. Ed. 44 (2005) 7053–7059.
[3] A.I. Cooper, Adv. Mater. 15 (2003) 1049–1059.
[4] K.P. Gierszal, M. Jaroniec, J. Am. Chem. Soc. 128 (2006) 10026–10027.
[5] S.H. Joo, S.J. Choi, I. Oh, J. Kwak, Z. Liu, O. Terasaki, R. Ryoo, Nature 414 (2001) 169–172.
[6] C.D. Liang, S. Dai, J. Am. Chem. Soc. 128 (2006) 5316–5317.
[7] H.J. Liu, S.H. Bo, W.J. Cui, F. Li, C.X. Wang, Y.Y. Xia, Electrochim. Acta 53 (2008) 6497–6503.
[8] X. Wang, P. Liu, Y. Tian, J. Solid State Chem. 184 (2011) 1571–1575.
[9] A.H. Lu, W.C. Li, A. Kiefer, W. Schmidt, E. Bill, G. Fink, F. Schuth, J. Am. Chem. Soc. 126 (2004) 8616–8617.
[10] A.H. Lu, W. Schmidt, N. Matoussevitch, H. Bonnemann, B. Spliethoff, B. Tesche, E. Bill, W. Kiefer, F. Schuth, Angew. Chem. Int. Ed. 43 (2004) 4303–4306.
[11] S. Yoon, J. Lee, T. Hyeon, S.M. Oh, J. Electrochem. Soc. 147 (2000) 2507–2512.
[12] S.W. Hwang, S.H. Hyun, J. Non-Cryst. Solids 347 (2004) 238–245.
[13] B. Xua, F. Wub, R. Chenb, G. Cao, S. Chen, Y. Yang, J. Power Sources 195 (2010) 2118–2124.
[14] B. Liu, H. Shioyama, H.L. Jiang, X.B. Zhang, Q. Xu, Carbon 48 (2010) 456–463.
[15] Y.Q. Dou, Y.P. Zhai, H.J. Liu, Y.Y. Xia, B. Tu, D.Y. Zhao, X.X. Liu, J. Power Sources 196 (2011) 1608–1614.

[16] H.J. Liu, X.M. Wang, W.J. Cui, Y.Q. Dou, D.Y. Zhao, Y.Y. Xia, J. Mater. Chem. 20 (2010) 4223–4230.

[17] M. Inagakia, H. Konnoa, O. Tanaike, J. Power Sources 195 (2010) 7880–7903.

[18] Y.K. Lv, M.X. Liu, L.H. Gan, Y.J. Cao, L.H. Chen, W. Xiong, Z.J. Xu, Z.X. Hao, H.L. Liu, L.W. Chen, Chem. Lett. 40 (2011) 236–238.

[19] N.D. Kim, W. Kim, J.B. Joo, S. Oh, P. Kim, Y. Kim, J. Yi, J. Power Sources 180 (2008) 671–675.

[20] A. Vinu, K. Ariga, T. Mori, T. Nakanishi, S. Hishita, D. Golberg, Y. Bando, Adv. Mater. 17 (2005) 1648–1652.

[21] Y. Xia, R. Mokaya, Adv. Mater. 16 (2004) 1553–1558.

[22] H.F. Li, R.D. Wang, Micropor. Mesopor. Mater. 111 (2008) 32–38.

[23] Y. Wang, L. Cheng, F. Li, H. Xiong, Y. Xia, Chem. Mater. 19 (2007) 2095–2101.

[24] L. Yu, C. Zhao, X. Long, W. Chen, Micropor. Mesopor. Mater. 126 (2009) 58–64.

[25] C. Sanchez, L. Rozes, F. Ribot, C. Laberty-Robert, D. Grosso, C. Sassoye, C. Boissiere, L. Nicole, C. R. Chimie 13 (2010) 3–39.

[26] L. Rozes, N. Steunou, G. Fornasieri, C. Sanchez, Monatsh. Chem. 137 (2006) 501–528.

[27] S. Eslava, F. Hengesbach, M. McPartlin, D.S. Wright, Chem. Commun. 46 (2010) 4701–4703.

[28] Y.K. Lv, C.H. Zhan, Y.L. Feng, CrystEngComm 12 (2010) 3052–3056.

[29] C.E. Sumner Junior, G.R. Steinmetz, J. Am. Chem. Soc. 107 (1985) 6124–6126.

[30] M. Sadakane, E. Steckhan, Chem. Rev. 98 (1998) 219–237.

[31] Y.K. Lv, Y.L. Feng, J.W. Liu, Z.G. Jiang, J. Solid State Chem. 184 (2011) 1339–1345.

[32] S. Melnic, D. Prodius, H. Stoeckli-Evans, S. Shova, C. Turta, Eur. J. Med. Chem. 45 (2010) 1465–1469.

[33] G.M. Sheldrick, SHELXS-97, Program for X-ray Crystal Structure Solution, University of Göttingen, Göttingen, Germany, 1997.

[34] G.M. Sheldrick, SHELXL-97, Program for X-Ray Crystal Structure Refinement, University of Göttingen, Göttingen, Germany, 1997.

[35] T. Ama, Md.M. Rashid, A.K. Saker, H. Miyakawa, T. Yonemura, H. Kawaguchi, T. Yasui, Bull. Chem. Soc. Jpn. 74 (2001) 2327–2333.

[36] G.A. Seisenbaeva, S. Gohil, V.G. Kessler, Inorg. Chem. Commun. 7 (2004) 18–20.

[37] A. Datta, W.S. Hwang, N. Revaprasadu, Inorg. Chem. Commun. 13 (2010) 671–675.

[38] S.H. Zhang, Y. Song, H. Liang, M.H. Zeng, CrystEngComm 11 (2009) 865–872.

[39] N.W. Ockwig, O. Delgado-Friedrichs, M. O'Keeffe, O.M. Yaghi, Acc. Chem. Res. 38 (2005) 176–182.

[40] L.F. Ma, Y.Y. Wang, L.Y. Wang, D.H. Lu, S.R. Batten, J.G. Wang, Cryst. Growth Des. 9 (2009) 2306–2308.

[41] S. Natarajan, P. Mahata, Chem. Soc. Rev. 38 (2009) 2304–2318.

[42] Y. Gogotsi, J. Chmiola, G. Yushin, C. Portet, P. Simon, P.L. Taberna, Science 313 (2006) 1760–1763.

[43] P. Simon, C. Largeot, C. Portet, J. Chmiola, P.-L. Taberna, Y. Gogotsi, J. Am. Chem. Soc. 130 (2008) 2730–2731.

[44] P. Simon, Y. Gogotsi, Philos. T. R. Soc. A 368 (2010) 3457–3467.

[45] D. Zhao, Q. Huo, J. Feng, B.F. Chmelka, G.D. Stucky, J. Am. Chem. Soc. 120 (1998) 6024–6036.

[46] A. Ōya, S. Ōtani, Carbon 17 (1979) 131–137.

[47] A.C. Ferrari, J. Robertson, Phys. Rev. B 61 (2000) 14095–14107.

[48] J. Schwan, S. Ulrich, V. Bathori, H. Erhardt, S.R.P. Silva., J. Appl. Phys. 80 (1996) 440–447.

[49] A. Oya, H. Marsh, J. Mater. Sci. 17 (1982) 309–322.